This article has been accepted for publication in a future issue of this journal, but has not been fully edited. Content may change prior to final publication. Citation information: DOI 10.1109/TIA.2016.2541616, IEEE Transactions on Industry Applications

Permanent Magnet Magnetization State Estimation Using High Frequency Signal Injection

Daniel Fernandez[1], David Reigosa[1], Juan Manuel Guerrero[1], Zi-Qiang Zhu[2], Fernando Briz[1]
[1]University of Oviedo. Dept. of Elect., Computer & System Engineering, Gijón, 33204, Spain.
[2] University of Sheffield. Department of Electronic and Electrical Engineering, UK.
fernandezalodaniel@uniovi.es, diazdavid@uniovi.es, guerrero@uniovi.es, z.q.zhu@sheffield.ac.uk, fernando@isa.uniovi.es

Abstract- Permanent magnet (PM) magnetization state estimation is important both for torque control and monitoring in conventional permanent magnet synchronous machines (PMSMs). Furthermore, this can be critical for variable flux machines (VFM). Use of high frequency signal injection methods for PM magnetization state estimation in NdFeB magnets has already been proposed. These methods make use of the variation of the PM high frequency resistance with the PM magnetization state due to the magnetoresistive effect. This paper address the generalization of magnetization state estimation using high frequency signal injection to other types of magnets like SmCo and ferrite, as well as to other magnet structures, e.g. isolated and non-isolated segmented magnets. Use of the magnetoresitive effect for the detection of irreversible/reversible PM demagnetization will also be shown to be viable.[1]

Index Terms — high frequency signal injection, permanent magnet magnetization state estimation, variable flux machines, segmented magnets.

I. Introduction

A variety of PMs have been used in electric machines, including Alnico, ferrite, SmCo and NdFeB. Although NdFeB rare earth permanent magnets are currently the primary option in high performance PMSMs [1-7], applications equipped with SmCo [8-9], AlNiCo magnets [10-12] and ferrite magnets [13-15] can also be found. More precisely, ferrite [6, 7], SmCo [8-9] or AlNiCo magnets combined with NdFeB magnets [10-12] are commonly used in VFMs [8-9]. Ferrite magnets are often used in low cost applications including domestic appliances, and STFMM for general purpose applications, with the goal of reducing cost (see Table I [16]) and the dependence on rare earth materials, at the price of a decrease of the machine performance. It is noted however that PM machines using ferrite magnets still provide higher performance than induction and synchronous reluctance motors [17].

TABLE I. Cost and Temperature Sensitivity of Different Magnetic Materials

Material	Alnico 8	Ferrite 9	SmCo 2:17	NdFeB 33EH	NdFeB 48M
$/Kg	35	15	100	200	150
a_B(%/ºC)	-0.01	-0.18	-0.035	-0.11	-0.12

PM magnetization state can vary during the normal operation of the machine due to the injection of *d*- and/or *q*-axis current and the temperature variation [20].

In most PMSMs, the *d*-axis current is used to weaken the PM flux [6-7], allowing constant power operation above base speed in SPMSM, IPMSM and STFMM, as well as to realize MTPA or other optimization strategies with IPMSM [1] and STFMM [10]. In addition, *d*-axis current is also used to permanently change the PM flux in VFM [8, 9].

PM magnetization state of ferrite, Alnico, SmCo and NdFeB also changes with temperature [18]. Table I shows typical values of the PM thermal remanent flux coefficient, α_B , which is defined as the rate of PM remanent flux variation with temperature [17-30]. The coefficient α_B is observed to vary significantly for different materials, PM field typically decreasing as the temperature increases [30]. Furthermore, even for the case of machines with identical design, assembling tolerances and minor differences in the magnet geometries and alloys may affect the machine magnetization state [31].

PM magnetization state estimation in PMSMs can be important for precise torque control and magnet state monitoring purposes of PM machine designs, including IPMSM, SPMSM, VFM or STFMM. In classical IPMSM and SPMSM, the magnetization state of the magnets can change, e.g. due to temperature. However, as shown in Table I, the variation of the magnetization state with temperature is relatively small. Consequently, the torque production capability of the machine will not change dramatically during normal operation, meaning that a highly precise magnetization state estimation will not be required for this type of machines. On the contrary, VFM and STFMM can be magnetized/demagnetized during normal operation of the machine, magnetization state estimation after this process [8] being critical.

PM magnetization state can be measured or estimated. Measuring the magnetization state once the machine is assembled is not easy. In SPMSMs, the PM field can be measured by inserting a magnetometer in the airgap. However, the machine end frame needs to be removed or alternatively drilled to insert the field sensor, in both cases the machine cannot operate normally. On the other hand, and to the best of authors' knowledge, no on-line PM field measurement system for IPMSMs, VFMs or STFMMs is available up to date.

Instead of PM field measurement, estimation methods can be used. PM magnetization state estimation methods can be divided into BEMF [13], pulse injection [21] and high frequency signal injection based methods [22]. BEMF and pulse injection methods estimate the PM magnetization state

[1] This work was supported in part by the Regional Ministry of Education, Culture and Sport of the Principality of Asturias through "Severo Ochoa Program" under Grant BP-13067.

978-1-4673-7151-3/15/$31.00 ©2015 IEEE

This article has been accepted for publication in a future issue of this journal, but has not been fully edited. Content may change prior to final publication. Citation information: DOI 10.1109/TIA.2016.2541616, IEEE Transactions on Industry Applications

from the stator flux linkage; both methods require the machine to be rotating, estimation at standstill being therefore not possible. High frequency signal injection based methods estimate the PM magnetization state from the PM electrical high frequency resistance, which changes with the magnetization state due to the magnetoresistive effect [23-27]. This method can be used over the whole speed range, including standstill. Magnetization state estimation using the magnetoresistive effect in PMSM using non-segmented NdFeB magnets has been reported in [22]. Although SmCo or ferrite magnets are commonly used in i.e. VFMs and STFMM, extension of the method to these magnet types remains unstudied.

This paper analyzes the magnetoresistive effect in SmCo and ferrite magnets. The study will also include segmented magnets, due to their importance for high speed machines [28], including electric vehicles [10]. Comparative analysis among the magnetoresistive properties of NdFeB, SmCo and ferrite magnets is also included.

The paper is organized as follows: physical principles of magnetoresistance effect in permanent magnets are presented in section II; the experimental setup used for magnetoresistance effect evaluation is presented in section III. High frequency signal injection for PM magnetization state estimation is presented in section IV, while experimental results are provided in section V. Finally the equivalence between the experimental setup for magnetoresistance effect evaluation and a PMSM is provided in section VI.

II. Magnetoresistive Effect in PMs

Magnetoresistance is defined as the change of the material's electrical resistance/resistivity with the application of a magnetic field [27]. For large electrical resistance variation (>10%) this effect is called giant magnetoresistance (GMR) [25, 26]. Magnetoresistance was initially discovered in thin-film structures alternating ferromagnetic and non-magnetic conductive layers. The effect was later also found in granular NdFeB magnets [25, 26]. This effect enables therefore NdFeB magnets to be used as a sensor that converts magnetic field changes into electrical resistance changes.

Magnetoresistance MR is defined by (1), where $R(0)$ is the resistance of the material in the absence of magnetic field, $R(\mathrm{H})$ (2) is the resistance of the material when a given magnetic field of strength H is applied, β is the sensitivity of the material resistance to an external field H.

$$MR = \frac{\Delta R}{R(0)} = \frac{\mathrm{R(H)} - R(0)}{R(0)} \quad (1)$$

$$R(\mathrm{H}) = R(0)(1+\beta(\mathrm{H}-\mathrm{H}_0)) = R(0)(1+\beta(\Delta \mathrm{H})) \quad (2)$$

Magnetic flux density B can be used instead of magnetic field strength H as it is the output of most field sensors; the relationship between both quantities being defined by (3), where μ_{CO} is the absolute permeability of the core.

$$H = \mu_{CO} B \quad (3)$$

Changes of PM electrical resistance can be estimated from the induced magnet eddy currents when an alternating magnetic field is applied to the PM [22]. The angle of the magnet surface, $\Theta_{B\text{-}I}$, respect to the external magnetic field vector (B_{ext}) will determine the relationship between the resistivity variation and the external magnetic field variation [27] (see Fig. 1). For the particular case of a PMSM, the eddy current vector can be assumed to be perpendicular to the electromagnetic field produced by the stator windings (see Fig. 2), the change of the material electrical resistivity due to the external magnetic field being therefore maximum, even with skewed machines.

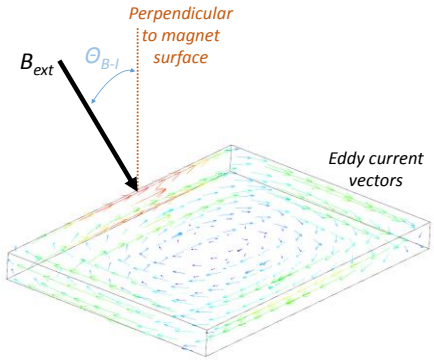

Fig. 1. External magnetic field, B_{ext}, and induced eddy currents vectors.

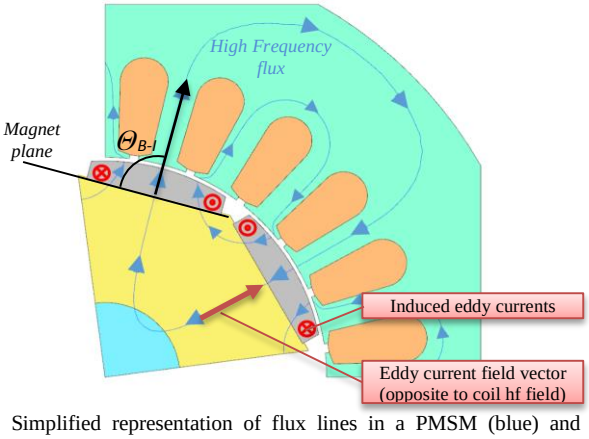

Fig. 2. Simplified representation of flux lines in a PMSM (blue) and magnet eddy current vectors (red).

In addition to the magnetoresistance effect, the PM electrical resistance also changes with temperature [22]. Both effects can be combined, the PM electrical resistance being expressed as (4) [22], where $R_{(T_0, B_{r-ini})}$ is the resistance at room temperature, T_0, $B_{r\text{-}ini}$ is the initial remanent PM flux, β is the coefficient that links the PM field variation and the resistance variation [18, 24, 25] and α_{mag} is the permanent magnet thermal resisitive coefficient.

$$\begin{aligned} R_{(\mathrm{T,B})} &= R_{(\mathrm{T_0,B_{r-ini}})}\left(1+\alpha_{mag}\Delta T + \beta \Delta \mathrm{B}\right) = \\ & R_{(\mathrm{T_0,B_{r-ini}})}\left(1+\alpha_{mag}(\mathrm{T}-\mathrm{T_0}) + \beta(\mathrm{B}-\mathrm{B_{r-ini}})\right) \end{aligned} \quad (4)$$

III. Experimental Setup for Measurement of Magnetoresistance Effect

Measurement of the magnetoresistive effect in the magnets of a PMSM is not easy due to the large number of design parameters that can affect the results [22], both in the stator (e.g. stator teeth shape, number of stator slots, number of poles...) and rotor (rotor geometry, number of PMs layers, PMs shape and size, flux barriers...). It is noted, however, that variations in the machine design will affect the sensitivity of its terminal properties (i.e. stator currents and voltages) to the magnetoresistance effect, but not to the magnetoresistance effect itself, since this is a property of the material.

This article has been accepted for publication in a future issue of this journal, but has not been fully edited. Content may change prior to final publication. Citation information: DOI 10.1109/TIA.2016.2541616, IEEE Transactions on Industry Applications

It is therefore advantageous to evaluate the magnetoresistive effect in the PM before it is mounted in the machine, provided that the conclusions remain valid for the PMSM case. The system shown in Fig. 3a has been developed for this purpose. It consists of a core made of iron powder blocks (BK8320-26 and CK2020-26, μ_r=26) [26]. Two different coils will be used: a 490 turns coil for magnet disks evaluation and a two series connected coils (335 turns) for segmented magnets evaluation. The dimensions of the magnet and the central column of the core perfectly match with each other (see Fig. 3b), minimizing therefore the flux leakage.

It is noted that in the platform shown in Fig. 3a, the applied external field is perpendicular to the eddy current vector and there is no airgap between the core and the magnet (see Fig. 3b). On the contrary, PMSM present an air-gap between stator and rotor. Consequently, the setup in Fig 3 will have a reduced equivalent reluctance, enhancing therefore the magnetoresistive effect.

The high frequency equivalent circuit of the platform shown in Fig. 3 is given in Fig. 4, where v^p_{hfp} and i^p_{hfp} is the coil high frequency voltage and current, R^p_{hfp} , R^p_{hfFEp} , and R^s_{hfs} are the coil, core and magnet high frequency resistances respectively, L_{hfp} and L_{hfs} are the coil and magnet high frequency inductances, ω_{hf} is the frequency of the high frequency signal, i^s_{hfs} is the magnet high frequency current (eddy current) and M_{ps} is the mutual coupling between the primary and the secondary. It will be shown later in section VI that R^p_{hfFEp} can be safely neglected due to the reduced eddy currents induced in the iron powder core [22].

The high frequency model of the experimental setup, see Fig. 4, is represented by (5)-(6), which corresponds to the transformer based model in Fig. 4. The secondary high frequency current (7) can be obtained from (6). Combining (7) and (5), (8)-(9) are obtained, the high frequency impedance being (10), its real component being (11). Assuming that the eddy currents are typically limited by the material resistance (i.e R_{hfs} >> L_{hfs}), (12) is finally obtained. The magnet high frequency resistance reflected in the primary terminals (coil terminals), R^p_{hfs} , is obtained from (13). It is noted that the the proposed method provides a lumped estimation of the magnet high frequency resistance and therefore of the magnet magnetization state.

$$v^p_{hfp} = \left(R^p_{hfp} + j\omega_{hf} L_{hfp}\right) i^p_{hfp} + j\omega_{hf} M_{ps} i^s_{hfs} \quad (5)$$

$$0 = \left(R^s_{hfs} + j\omega_{hf} L_{hfs}\right) i^s_{hfs} + j\omega_{hf} M_{ps} i^p_{hfp} \quad (6)$$

$$i^s_{hfs} = \frac{-j\omega_{hf} M_{ps} i^p_{hfp}}{\left(R^s_{hfs} + j\omega_{hf} L_{hfs}\right)} \quad (7)$$

$$v^p_{hfp} = \left(R^p_{hfp} + j\omega_{hf} L_{hfp}\right) i^p_{hfp} - j\omega_{hf} M_{ps} \frac{j\omega_{hf} M_{ps} i^p_{hfp}}{\left(R^s_{hfs} + j\omega_{hf} L_{hfs}\right)} \quad (8)$$

$$v^p_{hfp} = \left(R^p_{hfp} + j\omega_{hf} L_{hfp}\right) i^p_{hfp} + \frac{\omega^2_{hf} M^2_{ps}}{\left(R^s_{hfs} + j\omega_{hf} L_{hfs}\right)} i^p_{hfp} \quad (9)$$

$$Z_{hfp} = \frac{v^p_{hfp}}{i^p_{hfp}} = \left(R^p_{hfp} + j\omega_{hf} L_{hfp}\right) + \frac{\omega^2_{hf} M^2_{ps}}{\left(R^s_{hfs} + j\omega_{hf} L_{hfs}\right)} = \quad (10)$$

$$R_{hf} + j\omega_{hf} L_{hf}$$

$$R_{hf} = R^p_{hfp} + \frac{\omega^2_{hf} M^2_{ps} R^{s\ 2}_{hfs}}{R^{s\ 2}_{hfs} + \omega^2_{hf} L^2_{hfs}} \quad (11)$$

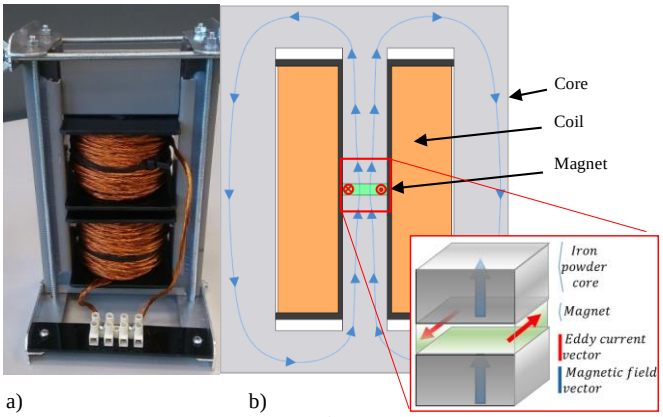

a) b)

Fig. 3. a) Experimental setup used for PM magnetoresitance evaluation and b) simplified representation of flux lines (blue) and magnet eddy current vectors (red) in the experimental setup.

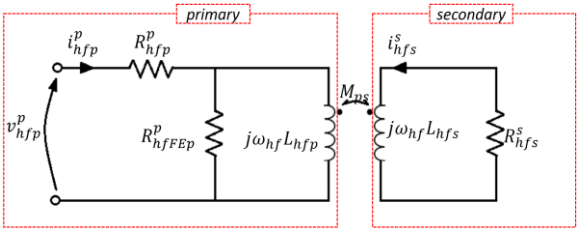

Fig. 4. Equivalent high frequency model of the simplified geometry.

$$R_{hf} = R^p_{hfp} + \frac{\omega^2_{hf} M^2_{ps}}{R^{s\ 2}_{hfs}} \quad (12)$$

$$R^p_{hfs} = \frac{\omega^2_{hf} M^2_{ps}}{R^{s\ 2}_{hfs}} = R_{hf} - R^p_{hfp} \quad (13)$$

IV. High Frequency Signal Injection for PM Magnetization State Estimation

Injection of a periodic high frequency signal has been shown to be a viable option for magnet high frequency resistance estimation [22]. Choosing the magnitude of the high frequency signal involves a tradeoff between the signal-to-noise ratio and induced magnet losses; lager magnitudes result in larger losses due to eddy current. However, it also increases the signal-to-noise ratio, which is advantageous for the practical implementation of the method. Choosing the frequency of the high frequency signal involves a tradeoff between the induced power losses and skin effect consideration. Induced magnet power losses can be expressed as (14), where B_m is the flux density, f_{hf} is the frequency of the injected signal, ρ is the resistivity of the magnet and K_e is a constant which depends on material size. It is observed from (14) that the losses are proportional to the square of the frequency of the injected signal and to the flux density. Skin depth can be calculated using (15), where δ is the skin depth, and μ_0 and μ_r are the magnetic permeability of the air and the magnet respectively. Generally speaking, the skin depth should be larger than the magnet height, otherwise there will be a loss in magnetoresistance sensitivity, as the eddy currents will only flow over a portion of the magnet height equal to the skin depth. The maximum frequency of the injected signal, f_{hf_max}, can be calculated using (16), and occurs when the skin depth is equal to the magnet height.

$$P = Ke \frac{(B_m\ f_{hf})^2}{\rho} \quad (14)$$

This article has been accepted for publication in a future issue of this journal, but has not been fully edited. Content may change prior to final publication. Citation information: DOI 10.1109/TIA.2016.2541616, IEEE Transactions on Industry Applications

$$\delta = \sqrt{\frac{2\rho}{2\pi f_{hf}\mu_0\mu_r}} \quad (15)$$

$$f_{hf\_max} = \frac{2r}{2\rho d^2 m_0 m} \quad (16)$$

Table II shows the magnet parameters and the maximum frequency of high frequency signal that will be used for the NdFeB, SmCo and ferrite disks to analyze (see Fig. 5).

TABLE II. MAGNET PARAMETERS

Magnet Type	*Height (mm)*	*Radius (mm)*	μ_r	ρ (Ωm)	f_{hf_max} (KHz)
NdFeB	5	10	1.05	1.44e-06	6.6
SmCo	5	10	1.05	85 e-06	4.0e2
Ferrite	5	10	1.05-1.10	1e3-1e4	2.0e3

Figure 6 schematically shows the signal processing used for magnet resistance estimation. The inputs are the primary voltage and current, v^p_{Lp} and i^p_{Lp}, and the stator primary (coil) high frequency resistance R_{hfp}. Two band-pass filters (*BPF1* and *BPF2*) are used to separate the high frequency voltage and current from the DC current, which is used to change the PM magnetization state.

Fig. 5. Ferrite, SmCo and NdFeB disks.

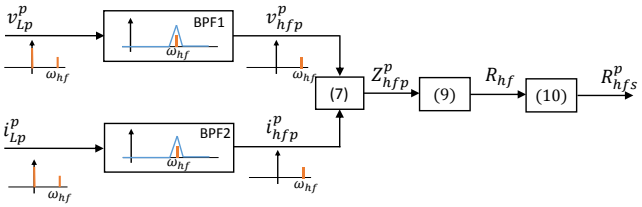

Fig 6. Signal processing used for magnet high frequency estimation using high frequency current/voltage injection.

V. EXPERIMENTAL RESULTS

A. *Signal injection*

Experiments were conducted using the geometry shown in Fig. 3. The coil is fed from a power converter as shown in Fig. 7. Table III shows the coil and power converter data. Fig. 6 shows the control block diagram for the injection of the DC current used to change the PM magnetization state and the high frequency signal used to estimate the magnet high frequency resistance. A PI regulator is used to control the DC current, the high frequency signal being added on top of the PI controller output voltage. A band-stop filter (*BSF1*) is used to remove the induced high frequency current in the coil to prevent the current regulator reaction to the injected high frequency signal.

Figs. 9a and 10a show an example of the injected voltage and current for the case of a DC current of 12 A and a high frequency voltage of 10 V. Figs. 9 and 10 show the applied voltage and the resulting current, as well as the corresponding frequency spectra. The DC and high frequency components at 250 Hz are readily observed. Though higher order components also exist, they are negligible (note the logarithmic scale in the frequency spectra).

The methodology for the experiment is as follows: The DC current and the high frequency voltage command are set simultaneously. Both DC and high frequency signals reach steady state in ≈30ms. After that, the high frequency resistance is estimated using the signal processing shown in Fig. 6. Estimation of the high frequency resistance takes ≈10ms, meaning that that the whole process takes ≈40ms.

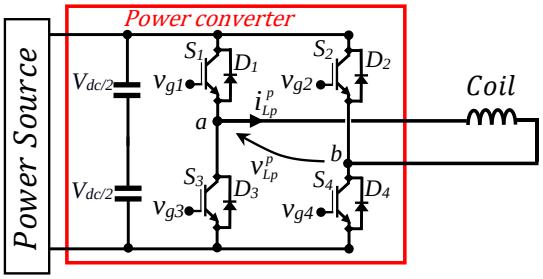

Fig. 7. H-Bridge power converter.

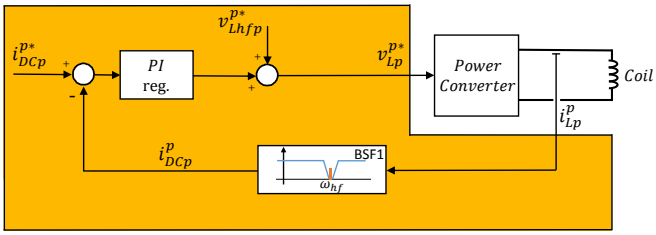

Fig. 8. Control block diagram of the DC and high frequency signal injection.

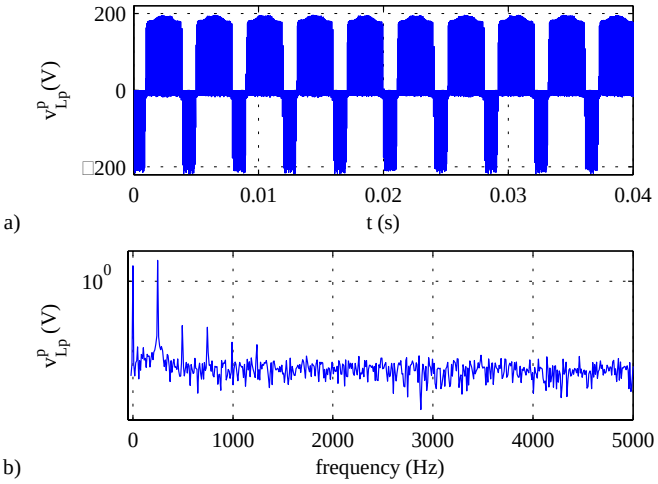

Fig. 9. a) Injected voltage (v^p_{Lp}), and c) corresponding frequency spectrum. I_{DC}=12A, f_{hf}=250Hz and V_{hf}=10V.

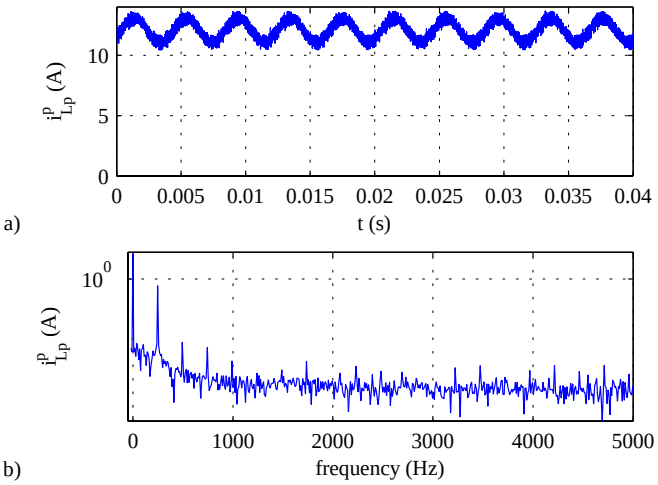

Fig. 10. a) Induced coil current (i^p_{Lp}), and b) corresponding frequency spectrum. Same operating conditions as in Fig. 9.

This article has been accepted for publication in a future issue of this journal, but has not been fully edited. Content may change prior to final publication. Citation information: DOI 10.1109/TIA.2016.2541616, IEEE Transactions on Industry Applications

TABLE III. EXPERIMENTAL SETUP PARAMETERS

Coil Parameters			Single Phase Rated Parameters	
	For Disks	For Segmented		
Number of Turns	335	490	Switching frequency	10 kHz
Resistance (Ω)	0.3236	0.6995	Voltage	380 V
Parallel wires per turn	14	7	Current	75 A
Inductance (mH)	5.2	12.5	*BSF1*	10Hz
α_{cu} (1/K)	3.9e-3	3.9e-3	Bandwidth Current reg.	200Hz

Both coil and magnet temperatures are measured before and after the test, the change of the magnet temperature during the experiment being negligible.

B. *Magnetoresistance of the coil and core*

Prior to the analysis of the magnetoresistive effect of the magnets, measurement of the magnetoresistance effect in the experimental coil and core is needed to further decouple these effects from the measurements. The total resistances *seen* from the coil terminals include coil, core and magnet resistance (see Fig. 4).

Figure 11 shows the measured high frequency resistances for the coil and the core. The coil high frequency resistance was measured by applying a high frequency voltage to the coil previous to the insertion of the coil in the core (i.e. air core coil). For the estimation of the core high frequency resistance, a high frequency voltage was applied to the coil terminals with the coil being mounted in the core as shown in Fig. 3. No magnet was inserted in the airgap in this case (see Fig. 9a). The H-Bridge is used to apply the coil a DC voltage and a high frequency voltage simultaneously. The DC voltage controls the DC current needed to change the magnetic flux density; the high frequency AC voltage, which is superposed on the DC voltage, is used for coil and core high frequency resistance estimation. The core high frequency resistance shows a peak at ≈-0.1T. This behavior is due to the fact that the iron powder core shows a small remanent magnetization when a high DC field is applied. The direction of this remanent magnetization produces the shift observed in Fig. 11.

It is observed from Fig. 11 that the coil with air core presents an almost constant high frequency resistance as the magnetic flux density changes, i.e. magnetoresistive effect being negligible. On the other hand, the high frequency resistance of the core slightly changes with the magnetic field, meaning that core presents relatively small magnetoresistive effect. However, this effect will be shown to be negligible when compared with the magnetoresistive effect in NdFeB magnets.

The magnetic flux density created by the injected DC current is measured by a Hall-effect mono-crystal gallium arsenide (GaAs) sensor [32]. Its measuring range is 0-3T. This is larger than the fields produced in the experimental setup and in PMSMs, which typically is in a range of 0-1.8T. Its maximum operating temperature being 125ºC. Location of the field sensor is shown in Fig. 12.

C. *Magnetoresistance effect in demagnetized samples*

This subsection analyzes the magnetoresistance effect in demagnetized magnet samples. The demagnetized PMs are inserted in the core as shown in Fig. 3 and 12b. NdFeB, SmCo and ferrite magnet disks will be evaluated (see Fig. 5). The magnets were initially fully demagnetized. Figure 13 shows the reflected magnet high frequency resistance of ferrite, NdFeB and SmCo disks. As for the experimental results of the core and coil magnetoresistance effect evaluation, a DC current (needed to create the magnetic field) and a high frequency voltage (needed for high frequency resistance estimation) are injected simultaneously. The magnetic field is measured by the field sensor (see Fig. 12b), the DC current being adjusted to produce the desired field. The core and coil high frequency resistances are decoupled from the overall estimated high frequency resistance, (11), using the data shown in Fig. 11.

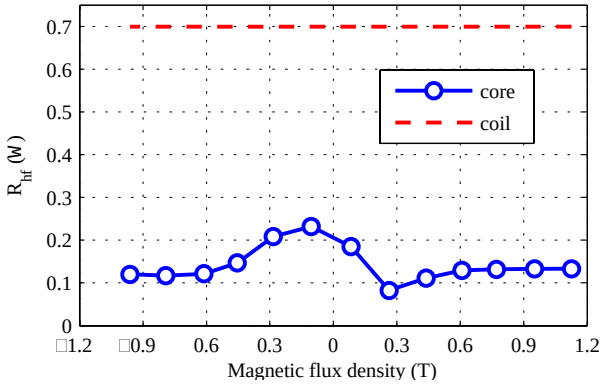

Fig. 11. Estimated high frequency resistance R^{p}_{hfs} of the iron powder core when the air-gap is equivalent to the height of the magnet, ○, and when there is no core, --. f_{hf}=250Hz and V_{hf}=0.05pu.

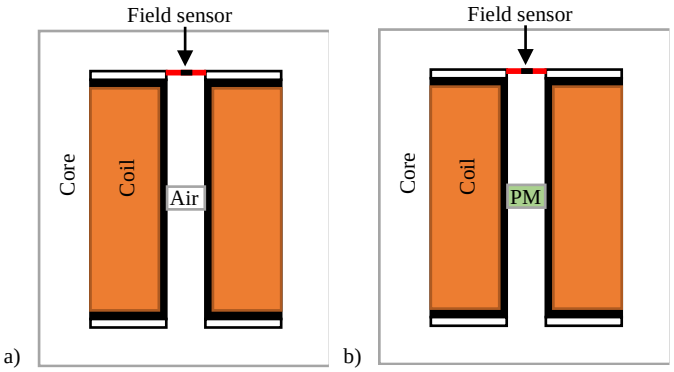

Fig. 12. Simplified representation of the experimental setup when the magnet is removed, a), and when the magnet is inserted, b). Placement of field sensor is indicated.

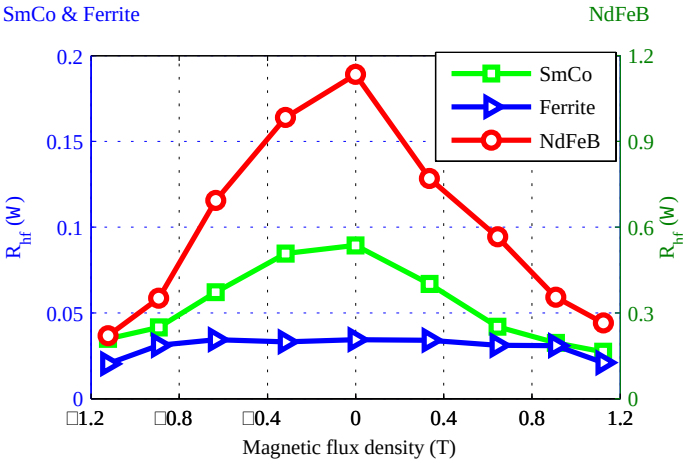

Fig. 13. Coil reflected magnet high frequency resistance, R^{p}_{hfs} of a ferrite ,▷, NdFeB, ○, and SmCo disks,□. f_{hf}=250Hz and V_{hf}=0.05pu

It is observed that, for the three magnet materials, the reflected magnet high frequency resistance decreases as the magnetic flux density (i.e. magnetization state) increases. NdFeB magnet shows the largest resistance variation, which is

This article has been accepted for publication in a future issue of this journal, but has not been fully edited. Content may change prior to final publication. Citation information: DOI 10.1109/TIA.2016.2541616, IEEE Transactions on Industry Applications

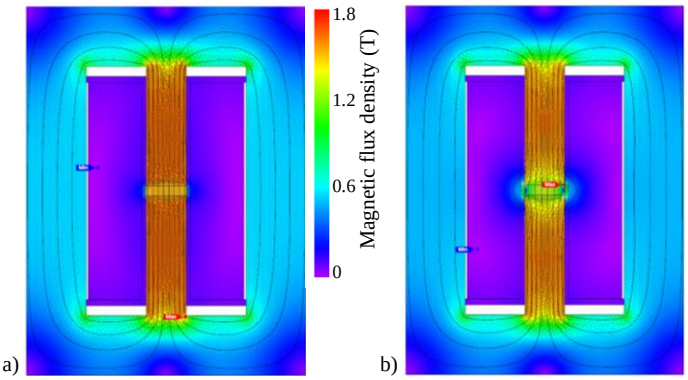

Fig. 14 FEA results showing the magnetic flux density when the DC current injected in the coil a) intensifies and b) weakens the magnet flux.

due to its iron composition [25, 26]. SmCo and ferrite magnets show a significantly reduced magnetoresistive effect. These results demonstrate that the magnetoresistive effect exists in ferrite, NdFeB and SmCo magnets, and that the variation of the magnet high frequency resistance can be used for magnetization state estimation.

D. *Magnetoresistance effect in magnetized samples*

This subsection analyzes the magnetoresistance effect in magnetized PMs. Figure 15 shows the reflected magnet high frequency resistance of ferrite, NdFeB and SmCo disks. The PMs were initially magnetized to the following magnetization states. NdFeB: ≈0, 0.25, 0.5, 0.75, 0.95 and ≈1.2T which correspond to ≈0.2, 0.4, 0.6, 0.8 and 1pu ; SmCo: ≈0,0.2, 0.4, 0.8T, which correspond to ≈0, 0.25, 0.5 and 1pu; ferrite:0, 0.25 and 0.35T, which correspond to 0, ≈0.7 and 1pu. The magnets are magnetized using the pulse magnetizer, shown in Fig. 16 the magnetization circuit parameters are shown in Table IV. Once the samples are magnetized, they are inserted in the core shown in Fig 3 and 12b. No DC current is injected in this case, the magnetic field shown in Fig. 15 therefore being due exclusively to the PM field, i.e. remanent flux. A high frequency signal is applied to the coil terminals for magnet high frequency resistance estimation. Comparing Fig. 13 and Fig. 15, similar tendencies for the demagnetized and magnetized samples are observed, the higher the magnetic flux density is, the lower is the reflected high frequency resistance. While magnetoresistance effect exists in all magnets, i.e. NdFeB, ferrite and SmCo, ferrite and SmCo are less sensitive to this effect than NdFeB, which is consistent with the experimental results obtained for the demagnetized samples shown in Fig. 13.

Finally, it is also observed from Fig. 13 that the estimated magnet high frequency resistance is asymmetric with respect to the zero magnetic flux density point (i.e. 0 T). The experimental setup used for this paper uses a single magnetic field sensor (see Fig. 12). Consequently, a uniform magnetic flux distribution in the core and PM is assumed. However, both magnetic fluxes in the core and the PM will be in general non-uniform, which can induce the asymmetric behavior in the estimated magnet high frequency resistance as observed in Fig. 13. Figs. 14a and 14b show the core and PM magnetic flux density contours obtained by FEA when the flux induced by the current injected in coil intensifies (Fig. 14a) or weakens (Fig. 14b) the magnet flux. As it can be observed, the field distribution on the magnet surface is not uniform, and cannot be measured therefore using a single field sensor (see Fig. 12). This produces an error between the measured and actual average magnet flux. It is also observed from Fig. 14b that a

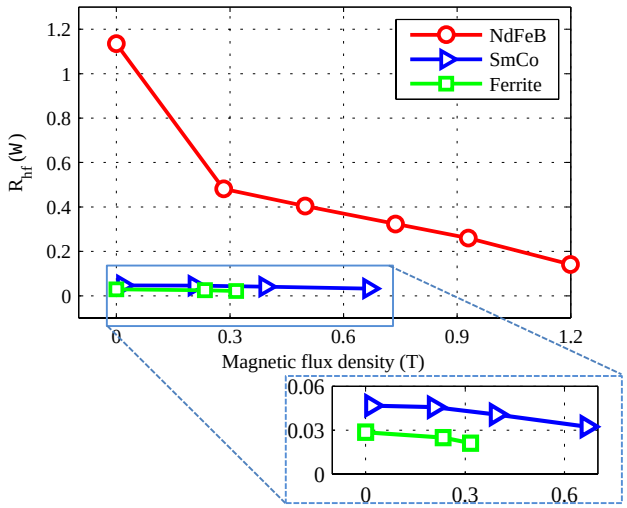

Fig. 15.Coil reflected magnet high frequency resistance for different values of the remanent field, and no DC current. for ferrite, (□), NdFeB (○) and SmCo (▷) disks f_{hf}=250Hz and V_{hf}=0.05pu

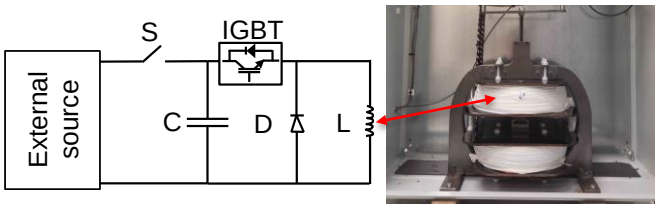

Fig. 16. Schematic representation of the circuit used for PM magnetization and demagnetization.

TABLE IV. MAGNETIZATION CIRCUIT PARAMETERS

External source max. voltage	750 V
Capacitor "C"	11750 μF
Diode "D"	1000 V, 1250 A
IGBT	1700 V, 1400 A
Coil "L"	1960 turns

flux leakage close to magnet edges exists. This flux leakage increases when a DC current is injected to weaken (or demagnetize) the PM and becomes zero when the PM magnetization direction changes.

E. *Magnetoresistance in magnetized samples combined with flux-weakening and flux-intensifying current*

This subsection analyzes the magnetoresistance effect in magnetized PMs combined with flux-weakening and flux-intensifying current injection. A DC current is being injected to decrease (partially counteract), i.e. flux-weakening current, or increase, flux-intensifying current, the PM field. As in the previous cases a high frequency signal is superposed to the DC current for PM high frequency resistance estimation.

For each initial magnetization state, the PM flux is weakened or intensified by injecting a DC current. It is observed that in all cases, the estimated magnet high frequency resistance decreases as the injected DC current increases, i.e. the magnetic flux density decreases or increases with respect to the magnet remanent flux. The expected behavior was that the magnetized samples would follow a similar behavior as the non-magnetized samples (see Fig. 15), the maximum magnitude of the high frequency resistance being obtained at zero magnetic flux density. This result was therefore unexpected and is a subject of ongoing research.

It is also observed that the estimated high frequency resistance when the PM field is counteracted by the DC current (and the resulting overall field is therefore null, i.e. temporary

This article has been accepted for publication in a future issue of this journal, but has not been fully edited. Content may change prior to final publication. Citation information: DOI 10.1109/TIA.2016.2541616, IEEE Transactions on Industry Applications

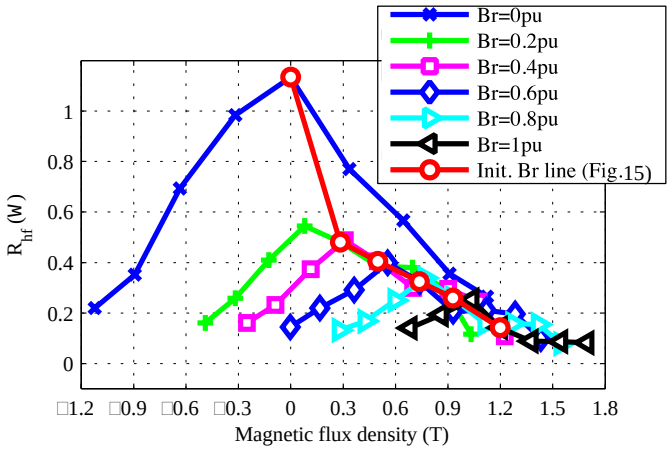

Fig. 17. Coil reflected magnet high frequency resistance for NdFeB magnets vs. the flux density, for different values of the remanent field. f_{hf}=250Hz and V_{hf}=0.05pu

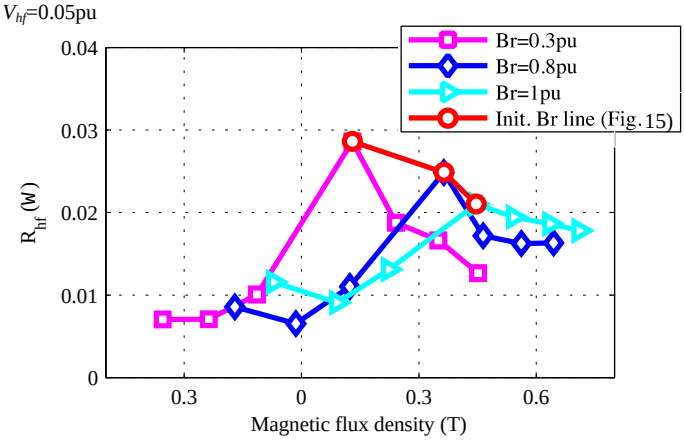

Fig 18. Coil reflected magnet high frequency resistance for a ferrite magnet vs. the flux density, for different values of the remanent field. f_{hf}=250Hz and V_{hf}=0.05pu.

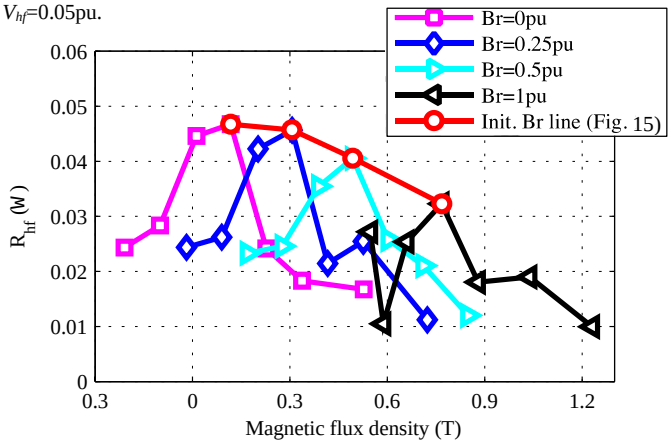

Fig 19. Coil reflected magnet high frequency resistance for a SmCo magnet. vs. the flux density, for different values of the remanent field. f_{hf}=250Hz and V_{hf}=0.05pu.

demagnetization) and when magnet is permanently demagnetized and no DC current is injected (see Fig 15) is different. This suggests that the estimated high frequency resistance allows to distinguish permanent and temporary demagnetization. This is a very interesting feature from a fault monitoring perspective. This is a subject of ongoing research.

It is concluded from the experimental results shown in Fig. 17-19 that the magnetoresistive effect exists in NdFeB, SmCo and ferrite magnets and that it can be potentially used for magnetization state estimation. It is also observed that the magnetoresistive effect produces larger high frequency resistance variations in NdFeB magnets than in SmCo and ferrite magnets. Consequently, magnetization state estimation in machines equipping SmCo and ferrite magnets might be more sensitive to signal-to-noise issues, AD converters resolution limits, etc.

F. Magnetoresistance effect in segmented magnets

The same experiments as for the disks magnets have been carried out for segmented NdFeB and SmCo magnets, see Fig. 20. Both isolated and non-isolated configurations have been used. Kapton tape (60μm) was used to isolate the magnets (Fig. 20).

Figure 21 shows experimental results for NdFeB segmented magnets with and without isolation, for magnet thickness of 5mm and 2.5 mm respectively. The PMs were initially demagnetized, the magnetic field being then changed by means of a DC current. As in the previous experimental results, a high frequency signal is superposed to the DC current for PM high frequency resistance estimation.

It is observed from Fig. 21 that the reflected magnet high frequency resistance is reduced by ≈60-70% when the magnets are isolated. It is also observed that the reflected magnet high frequency resistance decreases with the magnet thickness decrease, what reduces the sensitivity to the magnetoresistance effect. A reduction of the reflected magnet high frequency resistance (13), implies an increase of the actual magnet high frequency resistance, and consequently a reduction of the induced eddy currents in the magnets and of the induced losses. It is finally noted that for the segmented magnet case, the reflected magnet high frequency resistance is always smaller than for the magnet disk, even without insulation, see Figs. 13, 14 and 16.

Figure 22 shows the same experimental results as in Fig. 21 for SmCo 5mm segmented magnets. Experimental results using SmCo 2.5mm thickness magnets were not feasible due to magnetization/demagnetization limitations using the experimental setup shown in Fig. 16. The same conclusions as for the NdFeB are reached in this case.

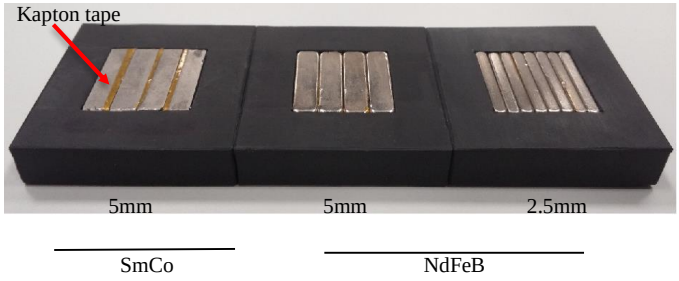

Fig 20. Segmented magnet arrangements (SmCo and NdFeB).

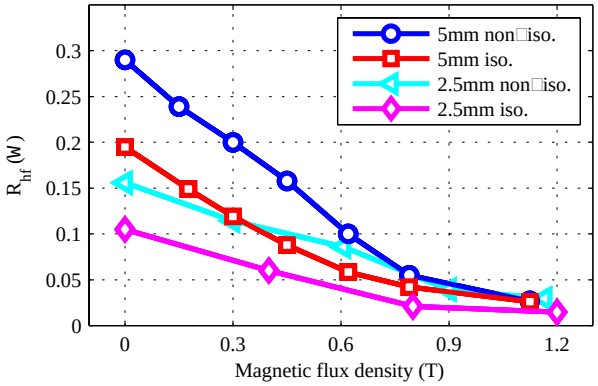

Fig 21. Coil reflected magnet high frequency resistance in 5mm and 2.5mm NdFeB segmented magnets when magnets are electrically isolated, □ and ▷, and when there is no electric isolation, ○ and ◊.

This article has been accepted for publication in a future issue of this journal, but has not been fully edited. Content may change prior to final publication. Citation information: DOI 10.1109/TIA.2016.2541616, IEEE Transactions on Industry Applications

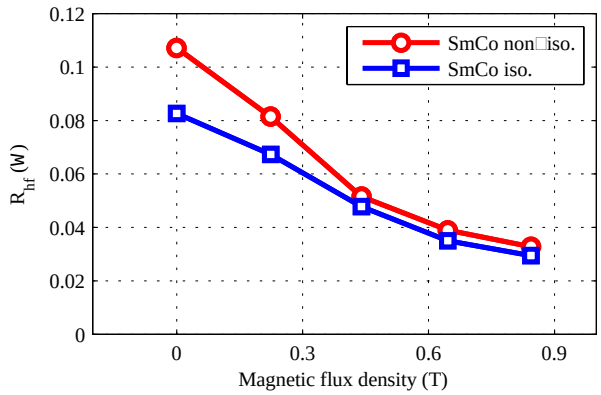

Fig 22. Coil reflected magnet high frequency resistance in 5mm SmCo segmented magnets when magnets are electrically isolated, ○, and when there is no electric isolation, □.

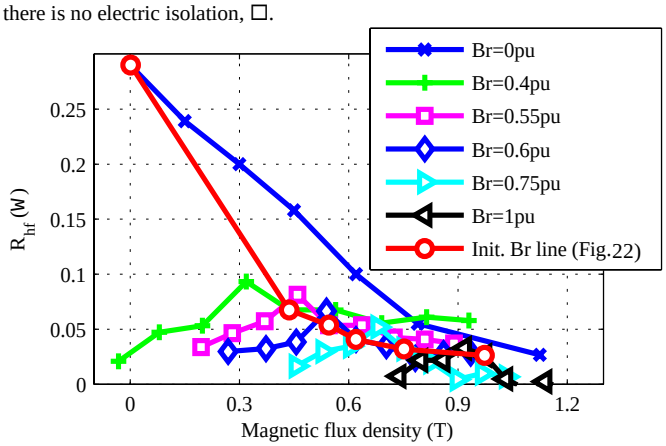

Fig. 23. Coil reflected magnet high frequency resistance, R^{p}_{hfs} of non-isolated segmented (5mm) NdFeB magnets. f_{hf}=250Hz and V_{hf}=0.05pu.

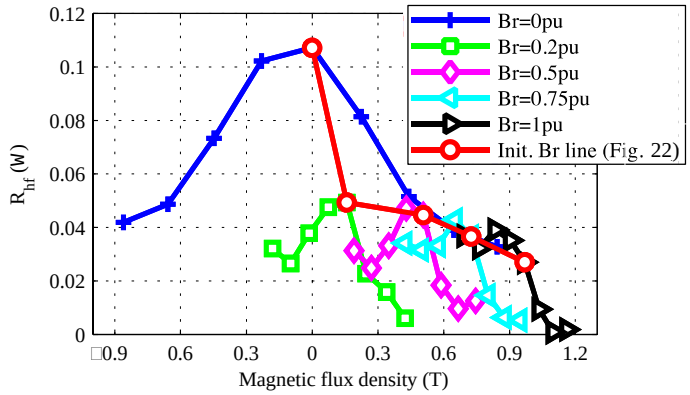

Fig. 24. Coil reflected magnet high frequency resistance, R^{p}_{hfs} of non-isolated segmented (5mm) SmCo magnets. f_{hf}=250Hz and V_{hf}=0.05pu.

Finally, Figs. 23 and 24 shows the same experimental results as in Figs. 17 and 19, but for the case of segmented magnets (5mm thickness). The same tendencies as in Figs. 17 and 19 are observed, the conclusions being consequently the same too. Experiments with 2.5 mm thickness NdFeB magnets showed the same behavior, they are not included. The slope of the curves shown in Fig. 13, 15, 17-19, 21-24 corresponds to the β coefficient in (4).

VI. Equivalence with a PMSM

Equivalences between the experimental setup presented in the previous section and the PMSM model, as well as potential application of the results to the PMSM case, are presented in this section.

Figure 25 shows the equivalent high frequency model of a PMSM [29] when a pulsating *d*-axis high frequency current is injected; v^{r}_{dshf} and i^{r}_{dshf} are the *d*-axis high frequency voltage and current, R_{dshf} is the stator winding *d*-axis high frequency resistance, L_{dshf} and L_{drhf} are the stator and rotor high frequency inductances, i^{r}_{drhf} is the rotor high frequency current (rotor lamination and magnet), M_{Dd} is the mutual coupling between stator and rotor *d*-axes, R_{drhf} is the rotor magnet high frequency resistance and R_{dshfFE} and R_{drhfFE} are the stator and rotor core high frequency resistances.

Comparing the equivalent circuits of the experimental setup in Fig. 4 and the PMSM in Fig. 25, the equivalence between both systems becomes evident. The only difference occurs in R_{dshfFE}, R_{drhfFE} and in for the two magnets (per pole pair) connected in series (i.e. two per pole-pair in the design shown in Fig. 2) in the rotor side of the PMSM. Table V summarizes the equivalences between the experimental setup and the PMSM. Consequently, it is realistic to assume that the results and conclusions obtained from the experimental platform can be extended to PMSMs. This assumption is also supported by the results presented in [22] which verified the method with IPMSM and SPMSM equipped with NdFeB magnets, since the magnetoresistive effect in NdFeB, SmCo and Ferrite magnets responds to the same principles.

Implementation of the method in an assembled machine would use the same scheme shown in sections IV and V. The high frequency signal voltage would be added in this case to the output voltage of the fundamental current regulator [3, 17-19, 22, 29], the signal processing being the same as in Fig. 6.

It is finally noted that this method is especially interesting in applications using machines in which magnetization state can be changed during normal operation, i.e. VFMs or STFMMs, magnetization state estimation being therefore critical in these machine types.

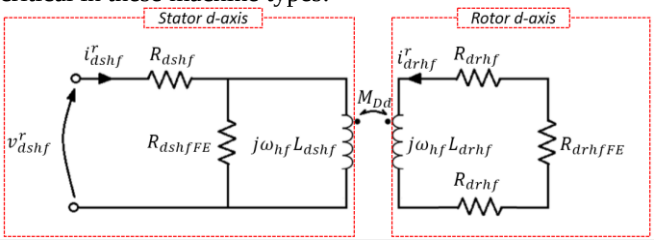

Fig. 25. Equivalent *d-axis* high frequency model of a PMSM.

TABLE V: Equivalences between Experimental Setup and a PMSM

Variables in the experimental setup high frequency model	Variables in the PMSM high frequency model
v^{p}_{hfp} : primary high frequency voltage	v^{r}_{dhf} : stator *d-axis* high frequency voltage
i^{p}_{hfp} : primary high frequency current	i^{r}_{dhf} : stator *d-axis* high frequency current
L_{hfp} : primary high frequency self-inductance	L_{dshf} : *d-axis* high frequency inductance
R^{p}_{hfp} : primary high frequency resistance	R_{dshf} : stator *d-axis* high frequency resistance
R^{p}_{hfFEp} : core high frequency resistance	R_{dshfFE} : stator core *d-axis* high frequency resistance
i^{s}_{hfs} : magnet high i^{r}_{drhf} frequency current	i^{r}_{drhf} : rotor core and magnet *d-axis* high frequency current
M_{ps} : mutual coupling between the primary and the secondary	M_{Dd} : mutual coupling between stator *d-axis* and rotor *d-axis*
L_{hfs} : secondary high frequency self-inductance	L_{drhf} : magnet high frequency self-inductance
R^{s}_{hfs} : secondary high frequency resistance	R_{drhf} : magnet high frequency resistance
Does not exists in the experimental setup	R_{drhfFE} : rotor core *d-axis* high frequency resistance

This article has been accepted for publication in a future issue of this journal, but has not been fully edited. Content may change prior to final publication. Citation information: DOI 10.1109/TIA.2016.2541616, IEEE Transactions on Industry Applications

VII. Conclusions

This paper presents a method to estimate the PM magnetization state, using the relationship between the PM electrical high frequency resistance and the PM magnetization state. The proposed method has been evaluated using NdFeB, SmCo and ferrite magnets, which are the most commonly used magnets in electrical machines.

Experimental verification has been conducted in an experimental setup using a simple geometry. This is advantageous for the analysis of the phenomena occurring in the magnet and the validation of the method. However, the equivalence between the experimental setup and the PMSM has been demonstrated, meaning the results from the experimental setup can be extrapolated to the PMSM case.

It has been concluded that the magnetoresistive can be used for magnetization state estimation in machines equipped with NdFeB, SmCo and ferrite magnets. It has also been shown that the estimated high frequency resistance can be potentially used to distinguish between permanent and temporal demagnetization, which is an important feature for fault prediction purposes.

VIII. References

[1] N. Limsuwan, Y. Shibukawa, D. Reigosa, M. Leetmaa and R.D. Lorenz, "Novel design of flux-intensifying interior permanent magnet synchronous machine suitable for power conversion and self-sensing control at very low speed," IEEE Trans. on Ind. Appl., vol.47, no.5, pp.2004–2012, Sept.-Oct. 2012

[2] K. Akatsu, M. Arimitsu, and S. Wakui, "Design and control of a field intensified interior permanent magnet synchronous machine," IEEJ Trans. Ind. Appl., vol.126, no.7, pp.827–834, Jul. 2006.

[3] S. Wu, D. Reigosa, Y, Shibukawa, M.A. Leetmaa, R.D. Lorenz and Y. Li, "IPM synchronous motor design for improving self-sensing performance at very low speed," IEEE Trans. on Ind. Appl., vol.45, no.6, pp.1939–1946, Nov.-Dec. 2009.

[4] N. Limsuwan, T. Kato, K. Akatsu and R.D. Lorenz, "Design and evaluation of a variable-flux flux-intensifying interior permanent-magnet machine," IEEE-ECCE, pp.3670-3677, Sept. 2012.

[5] T. Fukushige, N. Limsuwan, T. Kato and R.D. Lorenz, "Efficiency contours and loss minimization over a driving cycle of a variable-flux flux-intensifying interior permanent magnet machine," IEEE-ECCE, pp. 591-597, Sept. 2013.

[6] H. Liu, H. Lin, Z. Q. Zhu, M. Huang, and P. Jin, "Permanent magnet remagnetizing physics of a variable flux memory motor," IEEE Trans. on Magn., vol.46, pp.1679-1682, June 2010.

[7] K. Sakai, K. Yuki, Y. Hashiba, N. Takahashi, and K. Yasui, "Principle of the variable-magnetic-force memory motor," in Proc. of the Int. Conf. on Electrical Machines and Systems (ICEMS) 2009 Tokyo, 2009.

[8] B. Gagas, T. Fukushige, T. Kato and R. D. Lorenz,"Operating within Dynamic Voltage Limits during Magnetization State Increases in Variable Flux PM Synchronous Machines," IEEE-ECCE, pp.5206-6213, Setp. 2014.

[9] C. Y. Yu, T. Fukushige, A. Athavale, B. Gagas, K. Akatsu, D. Reigosa, R. D. Lorenz ,"Zero/low speed magnet magnetization state estimation using high frequency injection for a fractional slot variable flux-intensifying interior permanent magnet synchronous machine ," IEEE-ECCE, pp.2495-2502, Setp. 2014.

[10] H. Liu, A. Daikoku , N. Nishiyama, Y. Yoshikawa and Y. Kawazoe, "Recent technical trends in variable flux motors," Power Electronics Conference (IPEC-Hiroshima 2014 - ECCE-ASIA, pp.2011-2018, 2014

[11] A.Toba, H. Lin, S. Fang and X. Huang" Investigation of influence of permanent magnet shape on field-control parameters of variable flux memory motor with FEM," IEEE-WAC, pp.1-4, 2008.

[12] R. Owen, Z. Q. Zhu, J. B. Wang, D. A. Stone and I. Urquhart, "Review of variable-flux permanent magnet machines," IEEE-ICEMS, pp. 1-6 Aug.

[13] M.F. Hsieh, D. G. Dorrell, C. K. Lin, P. T. Chen, and Peter Y. P. Wung, "Modeling and effects of in situ magnetization of isotropic ferrite magnet motors," IEEE Trans. on Ind. Appl., vol.50, no.1, pp. 364-374, Jan. 2014.

[14] Wenliang Zhao; Lipo, T.A.; Byung-Il Kwon, "Comparative Study on Novel Dual Stator Radial Flux and Axial Flux Permanent Magnet Motors With Ferrite Magnets for Traction Application," in Magnetics, IEEE Transactions on , vol.50, no.11, pp.1-4, Nov. 2014

[15] S. Kim, J. Cho, S. Park, T. Park and S. Lim, "Characteristics comparison of a conventional and modified spoke-type ferrite magnet motor for traction drives of low-speed electric vehicles," IEEE Trans. on Ind. Appl.,vol.49, no. 6, pp. 2516-2522, Nov/Dec 2013

[16] www.arnoldmagnetics.com

[17] James D.Widmer, Richard Martin, Mohammed Kimiabeigi, "Electric vehicle traction motors without rare earth magnets," Elsevier, Sustainable Materials and Technologies. vol.3, pp. 7–13, Apr. 2015.

[18] D. Reigosa, F. Briz, P. García, J. M. Guerrero and M. W. Degner, "Magnet temperature estimation in surface PM machines using high frequency signal injection," IEEE Trans. on Ind. Appl., vol.46, no.4, pp.1468–1475, July-Aug. 2010.

[19] D. Reigosa, F. Briz, M. W. Degner, P. García and J. M. Guerrero, "Magnet temperature estimation in surface PM machines during six-step operation," IEEE Trans. on Ind. Appl., vol.48 no.6, pp.2353–2361, Nov.-Dec. 2012.

[20] D. Reigosa, F. Briz, M. W. Degner, P. García and J. M. Guerrero, "Temperature issues in saliency-tracking-based sensorless methods for PM synchronous machines," IEEE Trans. on Ind. Appl., vol.47, no.3, pp.1352–1360, May-June 2011.

[21] K. Liu, Q. Zhang, J. Chen, Z. Q. Zhu, and J. Zhang, "Online multiparameter estimation of nonsalient-pole PM synchronous machines with temperature variation," IEEE Trans. on Ind. Electr., vol.58, no.5, pp.1776-1788, May 2011.

[22] D. Reigosa, D. Fernandez, Z.Q. Zhu, F. Briz, "PMSM magnetization state estimation based on stator-reflected pm resistance using high frequency signal injection," IEEE Trans. on Ind. Appl., vol.51, no.5, pp.3800–3810, Sept.-Oct. 2015.

[23] W. Thomson, "On the electro-dynamic qualities of metals: Effects of magnetization on the electric conductivity of nickel and iron," Proc. Roy. SOC., 8: 546-550, 1857.

[24] T. R. McGuire and R.I. Potter, "Anisotropic magnetoresistance in ferromagnetic 3d alloys," IEEE Trans. on Magnetics, vol.11, no.4, pp.1018-1038, July 1975.

[25] B. Idzikowski, M. Wolf, A. Handstein, K. Nenkov, F. Stobieski and K.-H. Muller, "Inverse giant magnetoresistance in granular Nd/sub 2/Fe/sub 14/ B a-Fe," INTERMAG Magnetics Conference, Oct. 1997.

[26] B. Idzikowski, M. Wolf, A. Handstein, K. Nenkov, F. Stobieski and K.-H. Muller, "Inverse giant magnetoresistance in granular Nd2Fe14 B/α-Fe," IEEE Trans. on Magnetics, vol. 33, no. 5, pp. 3559-3561, Sept. 1997.

[27] S. O. Kasap, "Principles of electronic materials and devices," Third Edition 2006, ISBN 0-07-295791-3.

[28] S. Duan, L. Zhou, J. Wang, "Flux weakening mechanism of interior permanent magnet synchronous machines with segmented permanent magnets," in Applied Superconductivity, IEEE Transactions on , vol.24, no.3, pp.1-5, June 2014

[29] L. Alberti, N. Bianchi and S. Bolognani, "High frequency dq model of a synchronous machine for sensorless control," IEEE-ECCE, pp.4147-4153, Sept. 2014.

[30] D. Reigosa, D. Fernandez, H. Yoshida, T. Kato, Fe. Briz, "Permanent magnet temperature estimation in PMSMs using pulsating high frequency current injection," IEEE Trans. on Ind. Appl., vol.51, no.4, pp.3159 – 3168, July-Aug. 2015.

[31] Mehnaz A. Khan, Iqbal Husain, Mohammed R. Islam, T. Kato, Jeffrey T. Klass, "Design of experiments to address manufacturing tolerances and process variation influencing cogging torque and back EMF in the mass production of the permanent magnet synchronous motors," IEEE Trans. on Ind. Appl., vol.50, no.1, pp.346–355, Jan-Feb. 2014.

[32] www.hallsensors.de/CYSJ106C.pdf